Available online at www.sciencedirect.com
SCIENCE DIRECT®
International Journal of Heat and Mass Transfer 48 (2005) 1022–1037
International Journal of HEAT and MASS TRANSFER
www.elsevier.com/locate/ijhmt

Absolute and convective instabilities in the incompressible boundary layer on a rotating disk with temperature-dependent viscosity

H.A. Jasmine *, J.S.B. Gajjar

Department of Mathematics, University of Manchester, Oxford Road, Manchester M13 9PL, UK

Received 5 September 2003
Available online 10 December 2004

Abstract

The absolute and convective instability of Von-Kármán rotating disk flow with a temperature dependence viscosity of the form $\mu' = \mu_\infty/[1 + \epsilon(T - T_\infty)/(T_\omega - T_\infty)]$ is investigated. With the use of a spectral method, the linear stability equations are formulated and then solved numerically. Solutions have been obtained for various values of the parameter ϵ which controls the temperature dependence of viscosity. It is established the stability of the flow is particularly sensitive to changes in viscosity and even for small positive values of ϵ the flow is much more unstable compared to the constant viscosity case.

1. Introduction

Rotating disk flow has been at the centre of a large number of theoretical and experimental studies in recent years. Flows with heat transfer have significant industrial applications. Von-Kármán [1] was the first to formulate the problem where he showed that the Navier–Stokes equations for steady incompressible viscous flow of an infinite rotating disk in a rigidly rotating fluid can be reduced to a set of ordinary differential equations which can then be solved numerically. Using a two series expansion, Cochran [2] improved the accuracy of numerical solutions and demonstrated that the flow throws the fluid near the disk radially outwards which consequently introduces an axial flow towards the disk to maintain continuity. Related flows of interest are those of Bödewadt [3] where the fluid is rotating but the disk is stationary, and that of Rogers and Lance [4] where the fluid is rotating with angular velocity different from that of rotating disk. Sparrow and Gregg [5] examined the heat transfer from a rotating disk to a fluid for an arbitrary Prandtl number. Taking the temperature difference between the rotating disk surface and the stationary fluid to vary as a power of the disk radius, Hartnett [6] investigated the effect of surface temperature variation on the heat transfer from the disk to the fluid.

All of the studies mentioned above were confined to the assumption of constant viscosity. But with temperature changes, viscosity can also undergo a significant change. To predict the behaviour of a flow properly, it is therefore necessary to consider viscosity variation for incompressible fluids. When the viscosity variation on temperature is taken into account, Gary et al. [7], Mehta and Sood [8] demonstrated substantial change

* Corresponding author.
E-mail addresses: hjasmine@ma.man.ac.uk (H.A. Jasmine), gajjar@ma.man.ac.uk (J.S.B. Gajjar).

0017-9310/$ - see front matter © 2004 Published by Elsevier Ltd.
doi:10.1016/j.ijheatmasstransfer.2004.07.036

Nomenclature

(r', θ, z')	dimensional cylindrical polar coordinates
(r, θ, z)	non-dimensional cylindrical polar coordinates
t'	dimensional time
t	non-dimensional time
$\mathbf{U}'$	dimensional velocity
(u, v, w)	non-dimensional velocity components
p'	dimensional pressure
p	non-dimensional pressure
μ'	dimensional viscosity
μ	Non-dimensional viscosity
μ_∞	free-stream viscosity
ρ_∞	free-stream density
T'	dimensional temperature
T	non-dimensional temperature
T_w	temperature on surface of disk
T_∞	free-stream temperature
C_p	specific heat constant
κ	thermal conductivity
Ω	angular speed of disk
L	typical radial length scale
$U_c = L\Omega$	velocity scale
$\nu = \mu_\infty/\rho_\infty$	kinematic viscosity
$R_e = U_c L/\nu$	Reynolds number
$R = R_e^{1/2}$	Reynolds number based on displacement thickness
$(F, G, H), P, S$	self-similar profiles for the velocity, pressure and temperature
$Z = zR$	boundary layer variable
Pr	Prandtl number
h_∞	outflow from boundary layer
$(\bar{u}, \bar{v}, \bar{w}), \bar{p}, \bar{T}$	velocity, pressure and temperature perturbations
$(\tilde{u}, \tilde{v}, \tilde{w}), \tilde{p}, \tilde{T}$	normal mode velocity, pressure and temperature perturbations
$\alpha = \alpha_i + \mathrm{i}\alpha_r$	complex wavenumber in radial direction
β	azimuthal wavenumber
$\omega = \omega_r + \mathrm{i}\omega_i$	complex frequency
$\bar{\omega} = \omega/R$	
$X = rR$	multiple-scaling coordinate
$\lambda^2 = \alpha^2 + \beta^2$	
$\bar{\alpha} = \alpha - i/R$	
$\gamma = \tan^{-1}(\beta/\alpha_r)$	wave-angle

in flow characteristics compared to the constant viscosity assumption. Kafoussias and Williams [9], Kafoussias and Rees [10], and Keller [11] studied the effects of temperature dependent viscosity on mixed and natural convection flows by considering the viscosity to vary as linear function of temperature or proportional to a linear function of temperature.

Hossain et al. [12] investigated the flow and heat transfer along a uniformly heated and impulsively rotating disk in a stationary fluid subjected to a transverse magnetic field with temperature dependent viscosity. The flow considered is laminar with viscosity $\mu' = \mu_\infty/[1 + \epsilon(T - T_\infty)/(T_\omega - T_\infty)]$ and it is shown that heat transfer and surface friction will be affected by the flow in the viscous sub-layer close to the disk surface. Wall and Wilson [13] demonstrate that for monotonically decreasing viscosity across the channel, the flow is destabilized by heating. Pinarbasi and Ozalp [14] studied the effect of temperature-dependent and shear-thining viscosity of a non-Newtonian fluid on the stability of a channel flow. Their result shows that the formation of shear layers can only take place in solutions where the viscosity decreases sufficiently quickly as temperature increases. Shevtsova et al. [15] examined the stability of a liquid bridge consisting of a fluid volume held between two differentially heated concentric disks separated by a distance when the dependence of viscosity on temperature is taken into account. The existence of standing and travelling waves is discussed. The flow of a viscous incompressible fluid of temperature dependent viscosity past a permeable wedge has been considered by Hossain et al. [16]. Chang and Chan [17] discussed the linear stability of mixed convection flow of two immiscible fluids with temperature dependent viscosity. The linear stability of a ridge of fluid subjected to a jet of air with temperature dependent viscosity has recently been investigated by Mckinley and Wilson [18]. Using a finite difference method, Hossain et al. [19] explored the effect of a temperature dependent viscosity on natural convection flow of a viscous incompressible fluid from a vertical wavy surface. The influence of temperature dependent viscosity on the flow along a channel with porous wall was recently analyzed by Ferro and Gnavi [20]. However, investigations relating to the stability of a rotating disk with temperature dependent viscosity have not been carried out as yet, which therefore is one of the aims of the current work.

In this paper, we shall study the linear absolute and convective instability of Von-Kármán rotating disk flow by taking the viscosity to be temperature dependent. The viscosity of the fluid is taken as an inverse linear function of temperature. The viscosity coefficient is assumed to be of the form $\mu' = \mu_\infty/[1 + \epsilon\ (T - T_\infty)/(T_\omega - T_\infty)]$ see Ling and Dybbs [21]. For liquids such as water and crude oil, this function is in excellent agreement with experimental data. The traditional linear stability equations are formulated. Then, the branch points where the group velocity $\frac{\partial\omega}{\partial\alpha}$ tends to zero are searched for in the complex wavenumber, α, and complex frequency, ω,

planes. The equations are solved numerically by employing a spectral method for different values of the parameter ϵ. When ϵ is equal to zero, our solution is the same as presented by Turkyilmazoglu and Gajjar [22] (hereafter referred to as TG) and Lingwood [23]. As the value of the parameter ϵ is increased, we show that the flow becomes more unstable.

This paper is organized as follows: Section 2 is devoted to the description of the problem and governing equations of the flow. The results are presented in Sections 3 and 3.1 for the basic flow, Section 3.2 for linear stability, Section 3.3 for absolute instability. Our conclusions follow in Section 4.

2. The basic equations

2.1. Governing equations of the flow

We take an infinite planar disk rotating with uniform angular velocity Ω about the vertical axis z, which passes through the centre of the disk. We consider the three dimensional boundary layer flow of an incompressible fluid. The basic equations in cylindrical polar coordinates (r', θ, z') and corresponding velocity $\mathbf{U}'$ governing the viscous fluid flow are:

$$\rho_\infty\left(\frac{\partial \mathbf{U}'}{\partial t'} + (\mathbf{U}'\cdot\nabla)\mathbf{U}'\right) = -\nabla p' + \nabla(\mu'\nabla\mathbf{U}'), \tag{1a}$$

$$\nabla\cdot\mathbf{U}' = 0, \tag{1b}$$

$$\rho_\infty C_p\left(\frac{\partial T'}{\partial t'} + (\mathbf{U}'.\nabla)T'\right) = k\nabla^2 T' \tag{1c}$$

Here, T' is the temperature, C_p is the specific heat at constant pressure, ρ_∞ the fluid density, κ the thermal conductivity of the fluid, p' the pressure, and μ' the viscosity of the fluid. In addition, we assume that the viscosity depends on temperature, as $\mu' = \mu_\infty/[I + \varepsilon(T' - T_\infty)/(T_\omega - T_\infty)]$, where ϵ is termed the viscosity variation parameter, T_ω denotes the uniform temperature at the disk surface and T_∞ is the temperature of the ambient fluid. All other material properties such as the fluid density ρ_∞ and the thermal conductivity κ of the fluid are treated as constants. The Navier–Stokes equations are non-dimensionalized with respect to a length scale L, velocity scale $U_c = L\Omega$, time scale L/U_C and pressure scale $\rho_\infty U_c^2$. This leads to a global Reynolds number $R_e = U_c L/\nu = R^2$ where R is the Reynolds number based on the displacement thickness $(\nu/\Omega)^{\frac{1}{2}}$. Thus, relative to non-dimensional cylindrical polar coordinates (r, θ, z) which rotate with the disk, and corresponding velocities (u, v, w) the full time-dependent, unsteady Navier–Stokes equations governing the viscous fluid flow are the usual momentum and the continuity equations given as follows:

$$\begin{aligned}&\frac{\partial u}{\partial t} + u\frac{\partial u}{\partial r} + \frac{v}{r}\frac{\partial u}{\partial \theta} + w\frac{\partial u}{\partial z} - \frac{v^2}{r} - 2u - r\\ &\quad= -\frac{1}{r}\frac{\partial p}{\partial r} + \frac{1}{R^2}\left[\frac{\partial}{\partial r}\left(\mu\frac{\partial u}{\partial r}\right) + \frac{\partial}{\partial r}\left(\mu\frac{u}{r}\right)\right.\\ &\qquad\left. + \frac{1}{r^2}\frac{\partial}{\partial \theta}\left(\mu\frac{\partial u}{\partial \theta}\right) + \frac{\partial}{\partial z}\left(\mu\frac{\partial u}{\partial z}\right) - \frac{2}{r^2}\frac{\partial}{\partial \theta}(\mu v)\right],\end{aligned} \tag{2a}$$

$$\begin{aligned}&\frac{\partial v}{\partial t} + u\frac{\partial v}{\partial r} + \frac{v}{r}\frac{\partial v}{\partial \theta} + w\frac{\partial v}{\partial z} + \frac{uv}{r} + 2u\\ &\quad= -\frac{1}{r}\frac{\partial p}{\partial r} + \frac{1}{R^2}\left[\frac{\partial}{\partial r}\left(\mu\frac{\partial v}{\partial r}\right) + \frac{\partial}{\partial r}\left(\mu\frac{v}{r}\right)\right.\\ &\qquad\left. + \frac{1}{r^2}\frac{\partial}{\partial \theta}\left(\mu\frac{\partial v}{\partial \theta}\right) + \frac{\partial}{\partial z}\left(\mu\frac{\partial v}{\partial z}\right) + \frac{2}{r^2}\frac{\partial}{\partial \theta}(\mu u)\right],\end{aligned} \tag{2b}$$

$$\begin{aligned}&\frac{\partial w}{\partial t} + u\frac{\partial w}{\partial r} + \frac{v}{r}\frac{\partial w}{\partial \theta} + w\frac{\partial w}{\partial z}\\ &\quad= -\frac{\partial p}{\partial z} + \frac{1}{R^2}\left[\frac{\partial}{\partial r}\left(\mu\frac{\partial w}{\partial r}\right) + \frac{1}{r}\frac{\partial}{\partial r}(\mu w)\right.\\ &\qquad\left. + \frac{1}{r^2}\frac{\partial}{\partial \theta}\left(\mu\frac{\partial w}{\partial \theta}\right) + \frac{\partial}{\partial z}\left(\mu\frac{\partial w}{\partial z}\right)\right],\end{aligned} \tag{2c}$$

$$\begin{aligned}&\frac{\partial T}{\partial t} + u\frac{\partial T}{\partial r} + \frac{v}{r}\frac{\partial T}{\partial \theta} + w\frac{\partial T}{\partial z}\\ &\quad= \frac{1}{R^2}\frac{1}{P_r}\left[\frac{\partial^2 T}{\partial r^2} + \frac{1}{r^2}\frac{\partial^2 T}{\partial \theta^2} + \frac{1}{r}\frac{\partial T}{\partial r} + \frac{\partial^2 T}{\partial z^2}\right],\end{aligned} \tag{2d}$$

$$\frac{\partial u}{\partial r} + \frac{u}{r} + \frac{1}{r}\frac{\partial v}{\partial \theta} + \frac{\partial w}{\partial z} = 0, \tag{2e}$$

where $\mu = 1/[1 + \varepsilon T]$ is the non-dimensional viscosity. Here the temperature has been non-dimensionalized as $T' = T_\infty + (T_w - T_\infty)T$. In this analysis the fluid is assumed to lie in the $z \geqslant 0$ semi-infinite space. In the above equations, streamline curvature effects as well as the effects stemming from the Coriolis force are present.

2.2. The mean flow equations

To obtain similarity solutions of the governing equations, these are first converted into a convenient form using appropriate transformations. The boundary layer coordinate Z, which is of order $O(1)$, is defined as $Z = zR$. Considering this, we can introduce the following mean flow variables:

$$u = rF(Z), \quad v = rG(Z), \quad w = \frac{1}{R}H(Z), \tag{3a}$$

$$p = \frac{1}{R^2}P(Z), \quad T = S(Z). \tag{3b}$$

Substituting (3) into (2) yields the following non-dimensional ordinary differential equations for the mean flow:

$$(1+\varepsilon S)F'' - \varepsilon S'F' - (1+\varepsilon S)^2[F^2 - (G+1)^2 + F'H] = 0, \tag{4a}$$

$$(1+\varepsilon S)G'' - \varepsilon S'G' - (1+\varepsilon S)^2[2F(G+1) + G'H] = 0, \tag{4b}$$

$$S'' - P_r S'H = 0, \tag{4c}$$

$$2F + H' = 0, \tag{4d}$$

where primes denote differentiation with respect to Z, and $P_r = \mu_\infty C_p/\kappa$ is the Prandtl number. The boundary conditions are

$$F = 0, \quad G = 0, \quad H = 0, \quad S = 1 \quad \text{at } Z = 0, \tag{5a}$$

$$F = 0, \quad G = -1, \quad S = 0, \quad \text{as } Z \to \infty. \tag{5b}$$

In addition the behaviour of the solutions for large Z suggest that $H \to h_\infty$, which implies a constant vertical velocity of the rotating fluid in the far-field above the disk. We solve the set of ordinary differential equations (4) subject to boundary conditions (5) with Prandtl number equal to 0.72 by employing a finite difference method and the Numerical Algorithms Group (NAG) library routine D02RAF.

2.3. Linear stability equations

We are here interested in perturbation solution of Von-Kármán's self-similarity velocity profiles. The instantaneous non-dimensionalized velocity components imposed on the basic steady flow are u, v, w, and the pressure component p and temperature T are such that

$$u(r,\theta,z,t) = rF(Z) + \bar{u}(r,\theta,z,t),$$

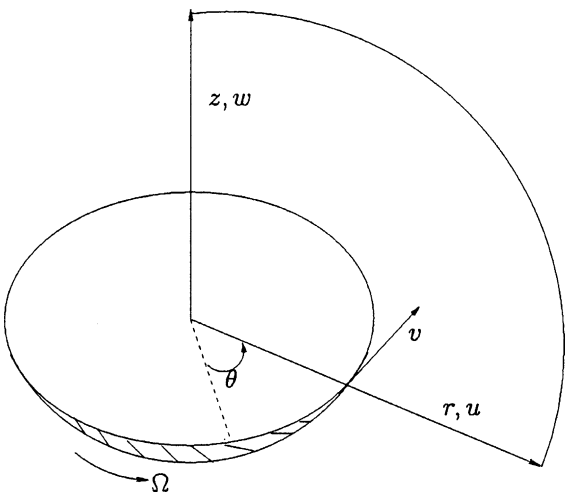

Fig. 1. A schematic of the flow configuration showing the non-dimensional coordinates (r,θ,z) and corresponding velocities (u,v,w).

$$v(r,\theta,z,t) = rG(Z) + \bar{v}(r,\theta,z,t),$$

$$w(r,\theta,z,t) = \frac{1}{R}H(Z) + \bar{w}(r,\theta,z,t),$$

$$p(r,\theta,z,t) = \frac{1}{R^2}P(Z) + \bar{p}(r,\theta,z,t),$$

$$T(r,\theta,z,t) = S(Z) + \overline{T}(r,\theta,z,t),$$

where $\bar{u}$, $\bar{v}$, $\bar{w}$, $\overline{T}$, and $\bar{p}$ are small perturbation quantities. The disturbance components of the above system are determined by solving the form of the Navier–Stokes equations that result from substituting these quantities into (2), and subtracting out the mean-flow equations. We linearize the equations for small perturbations. We find that the linearized Navier–Stokes operator has coefficients independent of θ and hence the disturbances can be decomposed into a normal mode form proportional to $e^{iR(\beta\theta - \omega t)}$. Such an approximation leads the disturbances to be wave-like, separable in θ and t. Consequently, the perturbations may be assumed to be of the form

$$(\bar{u},\bar{v},\bar{w},\bar{p},\bar{T}) = (\tilde{u}[r,Z],\tilde{v}[r,z],\tilde{w}[r,z], \tilde{p}[r,Z],\widetilde{T}[r,Z]e^{iR(\beta\theta-\omega t)} + \text{c.c.},$$

where β is the wavenumber in the azimuthal direction and ω the scaled frequency of the wave propagating in the disturbance wave direction. Here, c.c. denotes the complex conjugate.

The separation in θ and t simplifies the linear system of equations. However, no such simplification is possible as far as the r dependence is concerned (except in the limit as $R \to \infty$). The full linearized partial differential system has to be solved subject to suitable initial conditions to determine the stability of the flow. As in TG, we consider next the limit $R \to \infty$ and introduce the multiple-scale $X = Rr$ which is the appropriate scale on which the disturbances develop. After allowing for the multiple-scale replacement of $\frac{\partial}{\partial r}$ by

$$R\frac{\partial}{\partial X} + \frac{\partial}{\partial r},$$

and keeping only terms of $O(1/R)$, the following linear system is obtained

Table 1
Values of h_∞, $F'(0)$, $G'(0)$, and $S'(0)$ corresponding to different values of ϵ

ϵ	h_∞	$F'(0)$	$G'(0)$	$S'(0)$
0	−0.88447	0.5102	−0.6159	−0.3285
2	−0.59503	0.8833	−1.1097	−0.2866
4	−0.44875	1.1408	−1.4213	−0.2494
6	−0.3682	1.3501	−1.6708	−0.2216

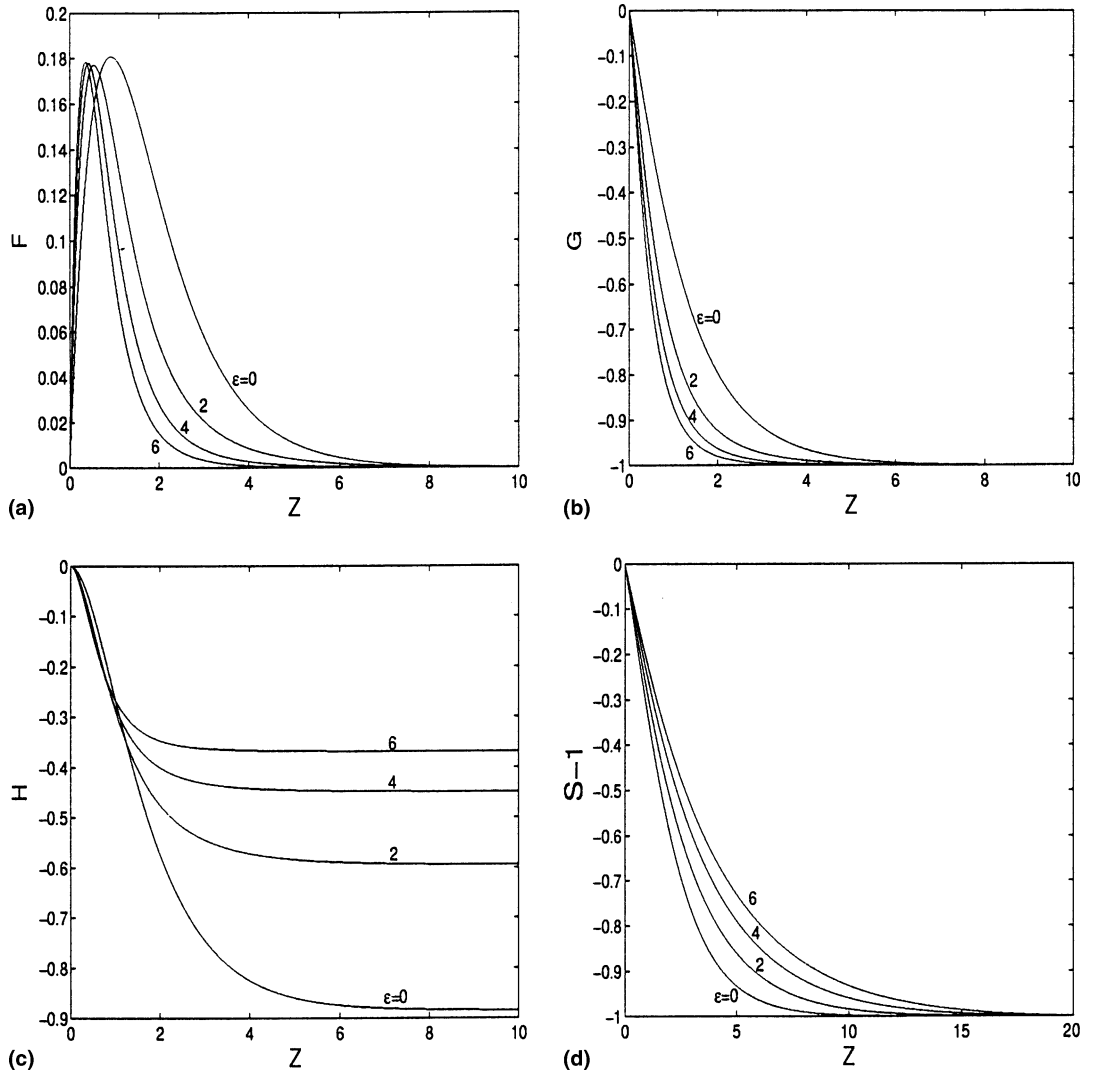

Fig. 2. Basic flow similarity profiles, (a) radial component $F(Z)$, (b) azimuthal $G(Z)$, (c) axial $H(Z)$, and (d) temperature profile $S(Z)$ against Z for different values of ϵ.

$$-\mathrm{i}\omega\tilde{u}+rF\frac{\partial\tilde{u}}{\partial X}+\mathrm{i}\beta G\tilde{u}+r\frac{\mathrm{d}F}{\mathrm{d}Z}\tilde{w}+\frac{\partial\tilde{p}}{\partial X}+\frac{1}{R}\left[\left(H+\frac{\varepsilon S'}{(1+\varepsilon S)^2}\right)\frac{\partial\tilde{u}}{\partial Z}+F\tilde{u}-2(G+1)\tilde{v}+-\frac{1}{(1+\varepsilon S)}\nabla_2^2\tilde{u}+\frac{\varepsilon F'\tilde{T}'}{(1+\varepsilon S)^2}-\left(\frac{2\varepsilon^2S'F'}{(1+\varepsilon S)^3}-\frac{r\varepsilon F''}{(1+\varepsilon S)^2}\right)\tilde{T}\right]=-\frac{1}{R}\left[rF\frac{\partial\tilde{u}}{\partial r}+\frac{\partial\tilde{p}}{\partial r}\right],\tag{6a}$$

$$-\mathrm{i}\omega\tilde{v}+rF\frac{\partial\tilde{v}}{\partial X}+\mathrm{i}\beta G\tilde{v}+r\frac{\mathrm{d}G}{\mathrm{d}Z}\tilde{w}+\frac{\mathrm{i}\beta}{r}\tilde{p}+\frac{1}{R}\left[\left(H+\frac{\varepsilon S'}{(1+\varepsilon S)^2}\right)\frac{\partial\tilde{v}}{\partial Z}+F\tilde{v}-2(G+1)\tilde{v}+-\frac{1}{(1+\varepsilon S)}\nabla_2^2\tilde{v}+\frac{\varepsilon G'\tilde{T}'}{(1+\varepsilon S)^2}-\left(\frac{2\varepsilon^2\theta'G'}{(1+\varepsilon S)^3}-\frac{r\varepsilon G''}{(1+\varepsilon S)^2}\right)\tilde{T}\right]=-\frac{1}{R}\left[rF\frac{\partial\tilde{v}}{\partial r}\right],\tag{6b}$$

$$-\mathrm{i}\omega\tilde{w} + rF\frac{\partial\tilde{w}}{\partial X} + \mathrm{i}\beta G\tilde{w} + \frac{\partial\tilde{p}}{\partial Z} + \frac{1}{R}\left[\left(H + \frac{\varepsilon S'}{(1+\varepsilon S)^2}\right)\frac{\partial\tilde{w}}{\partial Z} + \frac{\mathrm{d}H}{\mathrm{d}Z}\tilde{w} - \nabla_2^2\tilde{w}\right] = -\frac{1}{R}\left[rF\frac{\partial\tilde{w}}{\partial r}\right], \tag{6c}$$

$$-\mathrm{i}\omega\widetilde{T} + rF\frac{\partial\widetilde{T}}{\partial X} + \mathrm{i}\beta G\widetilde{T} + w\frac{\mathrm{d}S}{\mathrm{d}Z} + \frac{1}{R}\left[H\frac{\partial\widetilde{T}}{\partial Z} - \frac{1}{P_r}\nabla_2^2\tilde{w}\right] = -\frac{1}{R}\left[rF\frac{\partial\widetilde{T}}{\partial r}\right], \tag{6d}$$

$$\frac{\partial\tilde{u}}{\partial X} + \frac{1}{Rr}\tilde{u} + \frac{\mathrm{i}\beta}{r}\tilde{v} + \frac{\partial\tilde{w}}{\partial Z} = -\frac{1}{R}\frac{\partial\tilde{u}}{\partial r}. \tag{6e}$$

The operator ∇_2^2 is defined by

$$\nabla_2^2 = \frac{\partial^2}{\partial X^2} + \frac{\partial^2}{\partial Z^2} - \frac{\beta^2}{r^2}.$$

The basic flow is non-parallel in view of the terms on the right hand side of equations (6). Since these terms are of the order $O(1/R)$, when $R \to \infty$ and $i\alpha$ replaces $\frac{\partial}{\partial X}$, we get Rayleigh's equation. The full normal mode decomposition becomes valid only in this limit. Replacing $\frac{\partial}{\partial X}$ by $i\alpha$, setting $r = 1$, and neglecting terms of order $O(1/R)$ on the

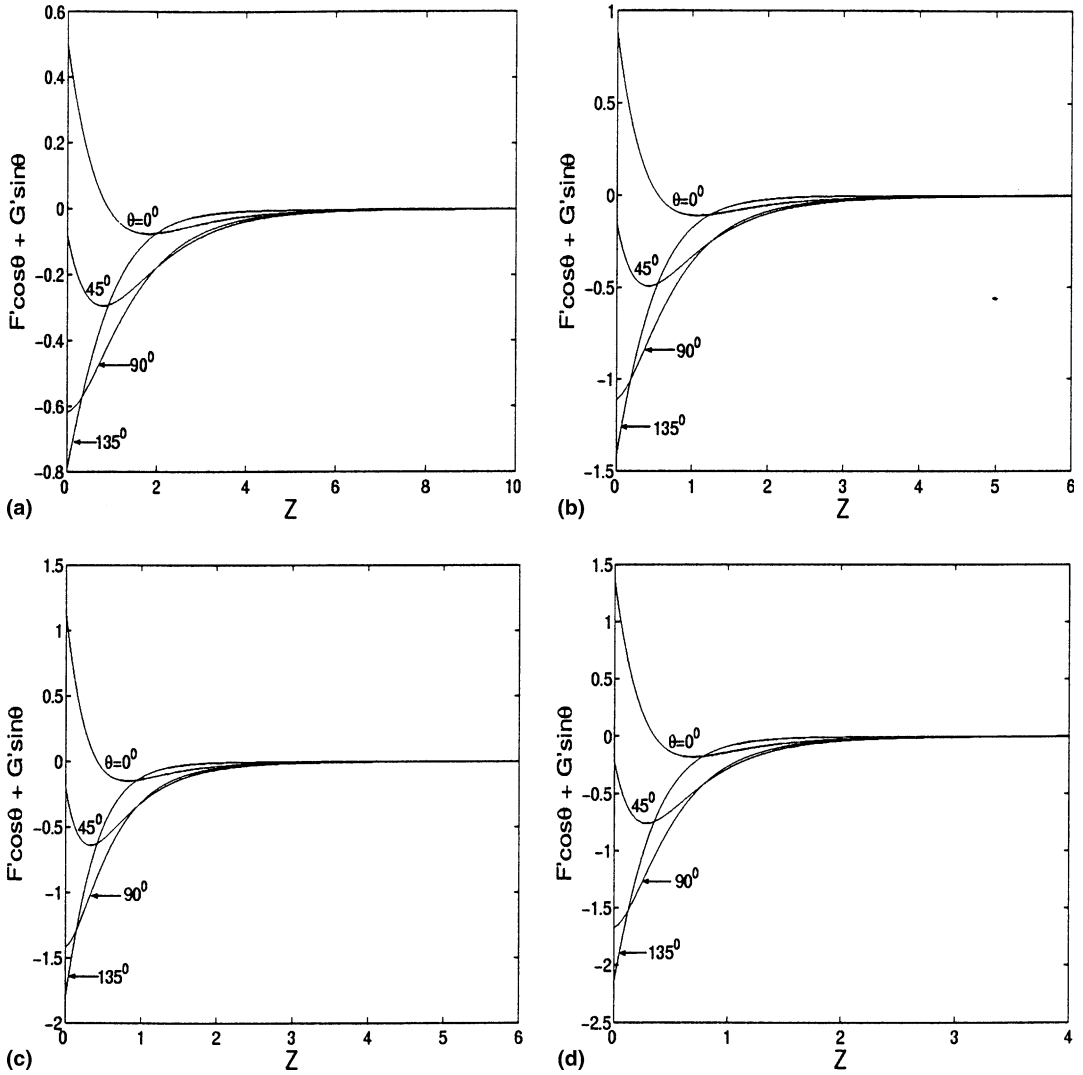

Fig. 3. Plots of the effective mean velocity ($F'\cos\theta + G'\sin\theta$) are shown for different values of θ: (a) $\epsilon = 0$, (b) $\epsilon = 2$, (c) $\epsilon = 4$, and (d) $\epsilon = 6$.

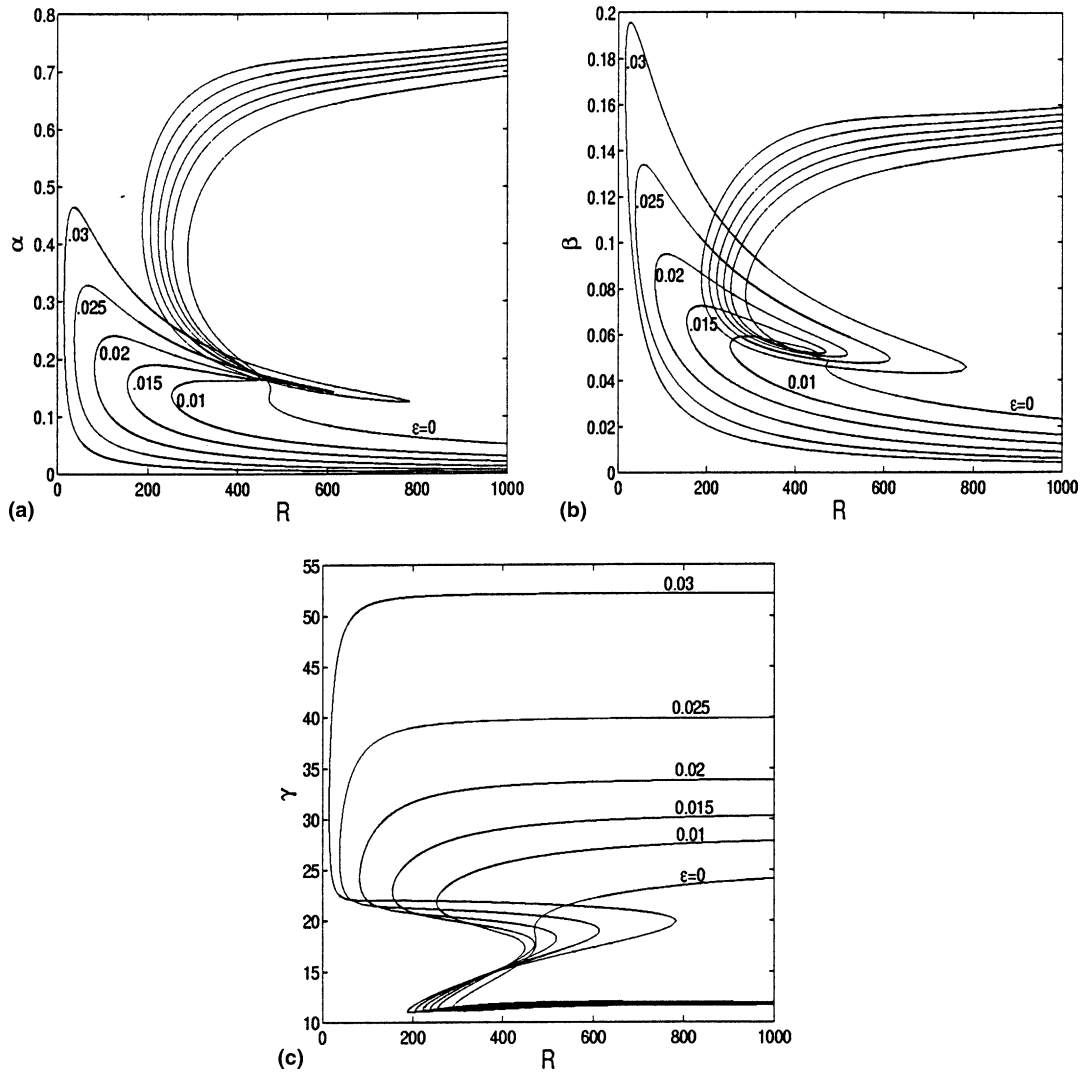

Fig. 4. Neutral stability curves in (a) (R,α), (b) (R,β) wavenumber, and (c) (R,γ) wave-angle planes for stationary waves, $\omega = 0$, and different values of ϵ.

Table 2
The values of the critical Reynolds number R, wavenumbers α and β, and wave angle γ corresponding to different values of ϵ on the upper branch for stationary waves with $\omega = 0$

ϵ	R	α	β	γ
0	287.2	0.3835	0.07735	11.40
0.01	255.0	0.3985	0.0800	11.36
0.015	239.1	0.4085	0.0817	11.31
0.02	222.7	0.4165	0.0829	11.26
0.025	205.7	0.4274	0.0844	11.18
0.03	187.7	0.4361	0.0853	11.07

Table 3
The values of the critical Reynolds number R, wavenumbers α and β, and wave angle γ corresponding to different values of ϵ on the lower branch for stationary waves with $\omega = 0$

ϵ	R	α	β	γ
0	451.4	0.1310	0.04645	19.50
0.01	253.4	0.1375	0.05515	21.85
0.015	155.1	0.1564	0.0661	22.91
0.02	82.6	0.1866	0.08414	24.27
0.025	38.0	0.2341	0.1159	26.35
0.03	15.1	0.2919	0.1738	30.77

right hand side of (6), the reduced linear system of equations are obtained. By replacing $\tilde{u}$, $\tilde{v}$, $\tilde{w}$, $\tilde{p}$, and $\widetilde{T}$ by u, v, w, p, and T, respectively, we have (Fig. 1)

$$\frac{1}{(1+\varepsilon S)}u'' - \left[H + \frac{\varepsilon S'}{(1+\varepsilon S)^2}\right]u' - \left[\mathrm{i}R(\alpha F + \beta G - \bar{\omega}) + \frac{\lambda^2}{(1+\varepsilon S)} + F\right]u + 2(G+1)v - RF'w - i\alpha R_p - \frac{\varepsilon F'T'}{(1+\varepsilon S)^2} + \left[\frac{2\varepsilon^2 S'F'}{(1+\varepsilon S)^3} - \frac{\varepsilon F''}{(1+\varepsilon S^2}\right]T = 0, \tag{7a}$$

$$\frac{1}{(1+\varepsilon S)}v'' - \left[H + \frac{\varepsilon S'}{(1+\varepsilon S)^2}\right]v' - \left[\mathrm{i}R(\alpha F + \beta G - \bar{\omega}) + \frac{\lambda^2}{(1+\varepsilon S)} + F\right]v - 2(G+1)v - RG'w - \mathrm{i}\beta R_p - \frac{\varepsilon G'T'}{(1+\varepsilon S)^2} + \left[\frac{2\varepsilon^2 S'G'}{(1+\varepsilon S)^3} - \frac{\varepsilon G''}{(1+\varepsilon S)^2}\right]T = 0, \tag{7b}$$

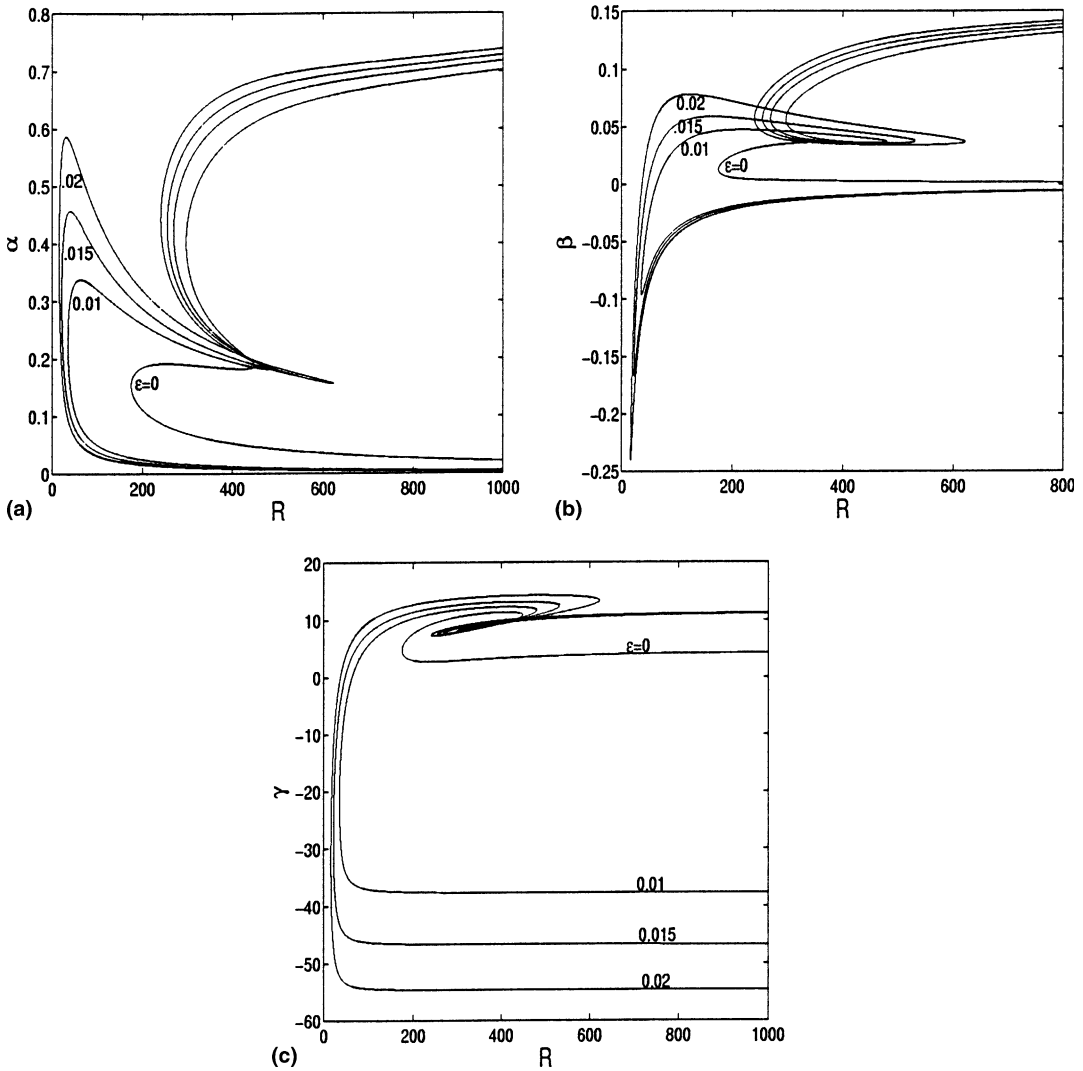

Fig. 5. Neutral stability curves in (a) (R,α), (b) (R,β), and (c) (R,γ) wavenumber and wave-angle planes for $\omega = 4$ and different values of ϵ.

$$\frac{1}{(1+\varepsilon S)}w'' - \left[H + \frac{\varepsilon S'}{(1+\varepsilon S)^2}\right]w' - \left[\mathrm{i}R(\alpha F + \beta G - \bar{\omega}) + \frac{\lambda^2}{(1+\varepsilon S)} + H'\right]w - R_{p'} = 0, \tag{7c}$$

$$T'' - P_r H T' - [\mathrm{i}RP_r(\alpha F + \beta G - \bar{\omega}) + \lambda^2]T - RS'P_r\omega = 0, \tag{7d}$$

$$\mathrm{i}\bar{\alpha}u + \mathrm{i}\beta v + w' = 0, \tag{7e}$$

where $\lambda^2 = \alpha^2 + \beta^2$, $\bar{\alpha} = \alpha - \frac{\mathrm{i}}{R}$, and $\bar{\omega} = \omega/R$. The boundary conditions for this set of equations are $u = v = w = T = 0$ at $Z = 0$, and $Z = \infty$.

3. Results

3.1. Mean flow results

We have solved the basic flow equations (4) by employing a finite difference method and the Numerical Algorithms Group (NAG) library routine D02RAF for $F(Z)$, $G(Z)$, $H(Z)$, and $S(Z)$. The values of h_∞, $F'(0)$, $G'(0)$, and $S'(0)$ corresponding to different values of ϵ are presented in Table 1. It is known that the viscosity of liquids decreases with increasing temperature. Therefore, an increase in viscosity variation parameter ϵ gives rise to a decrease in viscosity profile since ϵ signifies the sensitivity of the liquid to temperature. In Fig. 2(a), we plot the computed values of F versus Z for different values of ϵ. Fig. 2(a) reveals that an increase in the value of ϵ causes the point of maximum radial velocity to move

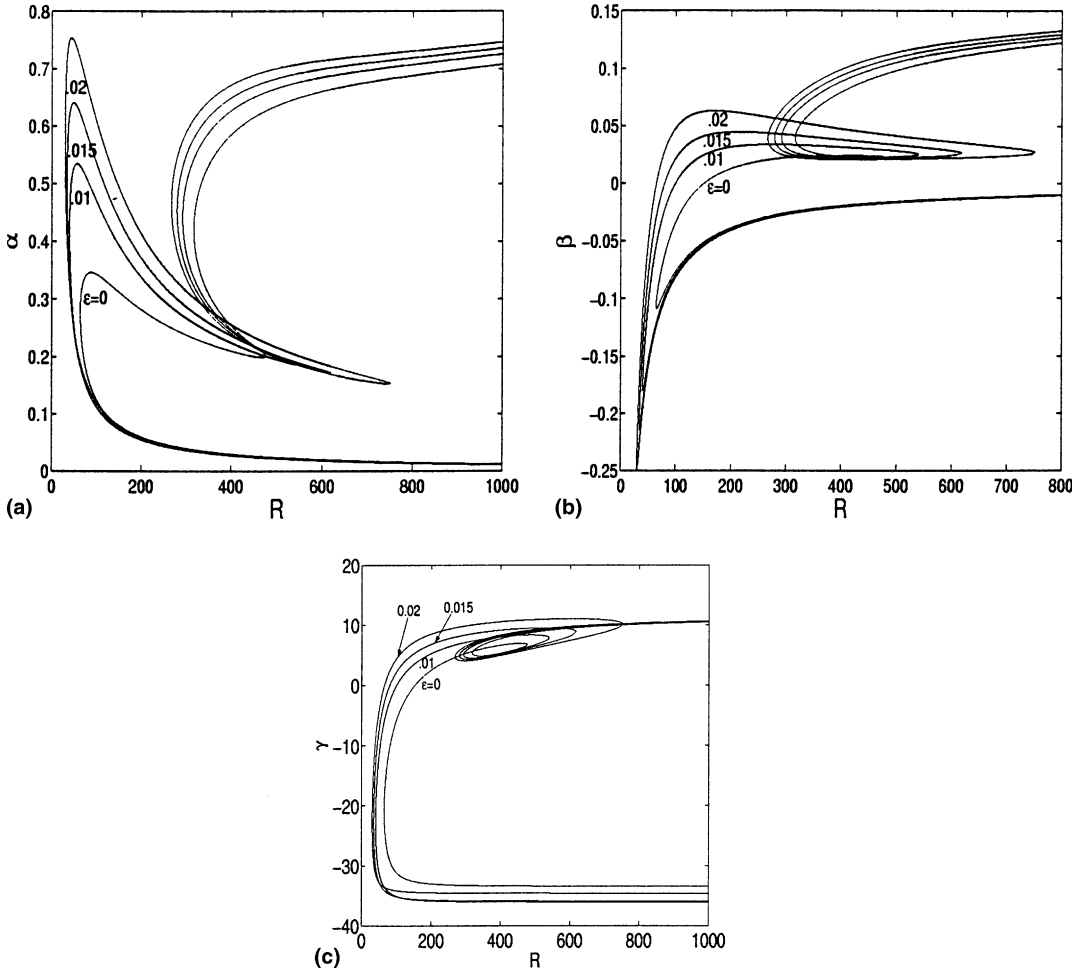

Fig. 6. Neutral stability curves in (a) (R, α), (b) (R, β), and (c) (R, γ) wavenumber and wave-angle planes for $\omega = 7.9$ and different values of ϵ.

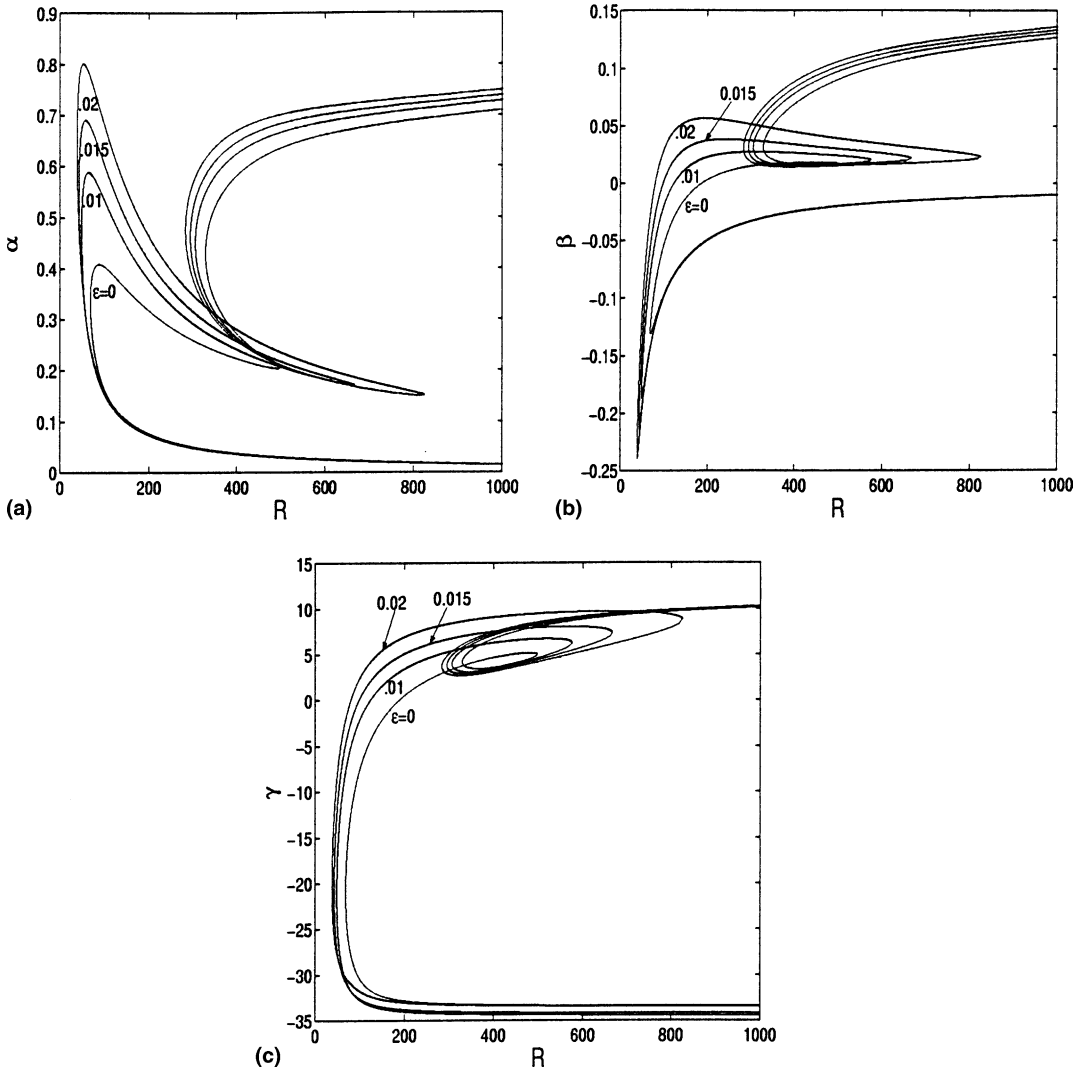

Fig. 7. Neutral stability curves in (a) (R,α), (b) (R,β) wavenumber, and (c) (R,γ) wave-angle planes for $\omega = 10$ and different values of ϵ.

Table 4
The values of the critical Reynolds number R, wavenumbers α and β, and wave angle γ corresponding to different values of ϵ on the lower branch for travelling waves with $\omega = 4$

ϵ	R	α	β	γ
0	297.6	0.4030	0.0563	7.9
0.005	283.8	0.4100	0.05642	7.8
0.01	269.7	0.4210	0.05698	7.7
0.015	255.4	0.4300	0.05698	7.5
0.02	241.0	0.4443	0.05756	7.3

Table 5
The values of the critical Reynolds number R, wavenumbers α and β, and wave angle γ corresponding to different values of ϵ on the lower branch for travelling waves with $\omega = 4$

ϵ	R	α	β	γ
0	175.2	0.1537	0.01273	4.73
0.005	76.8	0.1759	−0.02384	−7.71
0.01	35.3	0.2307	−0.09261	−21.87
0.015	30.4	0.3041	−0.1644	−28.40
0.02	16.1	0.3782	−0.2358	−31.94

closer to the surface of the disk. The velocity profiles G in the azimuthal direction versus Z for different values of ϵ are shown in Fig. 2(b). The velocity profiles in the axial direction for different values of ϵ are plotted in Fig. 2(c). It is clear that increasing ϵ decreases the magnitude of the outflow at the edge of the boundary layer. Overall

Table 6
The values of the critical Reynolds number R, wavenumbers α and β, and wave angle γ corresponding to different values of ϵ on the upper branch for travelling waves with $\omega = 7.9$

ϵ	R	α	β	γ
0	316.5	0.4210	0.0391	5.30
0.01	291.8	0.4422	0.03926	5.07
0.015	279.4	0.4547	0.03923	4.93
0.02	267.0	0.4659	0.03872	4.75

Table 7
The values of the critical Reynolds number R, wavenumbers α and β, and wave angle γ corresponding to different values of ϵ on the lower branch for travelling waves with $\omega = 7.9$

ϵ	R	α	β	γ
0	64.4	0.2773	−0.1064	−21.0
0.01	40.4	0.4211	−0.1772	−22.86
0.015	34.3	0.4981	−0.2111	−22.96
0.02	29.9	0.5812	−0.2442	−22.79

Fig. 2(a)–(c) suggest that increasing ϵ makes the boundary layer 'thinner' in some sense. In Fig. 2(d), we sketch the computed values of temperature profile S versus Z for different values of ϵ. The temperature profiles are much fuller for increasing values of the viscosity variation parameter ϵ. Our results for the mean flow agree well with the results obtained by Hossain et al. [12].

In Fig. 3, we plot a combination of $F'\cos\theta + G'\sin\theta$ versus $Z$for different values of θ with $\epsilon = 0, 2, 4, 6$, respectively. The quantity $F'\cos\theta + G'\sin\theta$ is the effective mean velocity at an angle θ and is important in the stability context. Even small changes in ϵ causes considerable change to this profile as compared to the $\epsilon = 0$ case, and this suggests that the stability of the mean flow will be particularly sensitive to changes in ϵ.

Table 8
The values of the critical Reynolds number R, wavenumbers α and β, and wave angle γ corresponding to different values of ϵ on the upper branch for travelling waves with $\omega = 10$

ϵ	R	α	β	γ
0	329.3	0.428	0.0313	4.10
0.01	306.3	0.4523	0.0315	3.98
0.015	294.8	0.4633	0.0311	3.84
0.02	283.5	0.4768	0.0309	3.71

Table 9
The values of the critical Reynolds number R, wavenumbers α and β, and wave angle γ corresponding to different values of ϵ on the lower branch for travelling waves with $\omega = 10$

ϵ	R	α	β	γ
0	68.7	0.3358	−0.1288	−20.98
0.01	49.8	0.4781	−0.1836	−21.01
0.015	42.8	0.5561	−0.2096	−20.65
0.02	38.3	0.6401	−0.2347	−20.14

3.2. Stability results

Having discussed the properties of the mean flow, we next analyze the stability of this flow. Two types of instability waves exist in the rotating disk boundary layer flow. The first one is the inviscid-type or the upper branch and the other one is the viscous-type or the lower branch. We have studied these two distinct branches for several values of the viscosity variation parameter ϵ with the Prandtl number taken equal to 0.72. First we consider stationary waves, i.e. disturbances with $\omega = 0$. Stability computations reported here have been done by using a spectral method (similar to that described in TG). The wave-angle γ of a disturbance is defined as $\gamma = \tan^{-1}(\beta/\alpha_r)$. In Fig. 4, we display the neutral curves for stationary disturbances in the (R,α), (R,β), and (R,γ) planes for several values of ϵ. The computed values of the critical Reynolds number R, the corresponding wavenumbers α and β, and wave-angle γ are tabulated in Table 2 for the upper branch and Table 3 for the lower branch. The data shows that an increase in the value of ϵ leads to a decrease in the values of the critical Reynolds numbers and wave-angle. Fig. 4(c) shows that the range of wave-angle decreases for the upper branch while increases considerably for the lower branch compared with $\epsilon = 0$ case. Fig. 4 also demonstrate that with increasing ϵ, the curves shift to the left and the flows become more unstable. For fixed Reynolds numbers, the band of unstable wavenumbers increases and the range of unstable wave-angles is increased considerably from the $\epsilon = 0$ case. The pattern of behaviour here may be explained by the behaviour of the effective mean velocity profile for increasing ϵ with the point of zero shear stress moving closer to the wall. The latter influences the dynamics on the lower-branch of the instability curve as shown by Hall [24].

Next, we consider travelling waves i.e. disturbances with non-zero values of frequency ω. The marginal curves for convective instability for non-stationary waves in the (R,α), (R,β), and (R,γ) plans are shown in Figs. 5–7 for several positive non-dimensional frequencies and for several values of ϵ. Fig. 5 shows the marginal curves for convective instability when $\omega = 4$ and different values of ϵ are taken. The computed values of R, α, β and γ are presented in Table 4 for the upper branch and Table 5 for the lower branch. For $\omega = 7.9$, Fig. 6 displays the neutral stability curves for different values of ϵ. The computed values of R, α, β and γ are tabulated in Table 6 for the upper branch and Table 7 for the lower. The critical values of R and γ decrease

while α shows increase as ϵ is increased. Fig. 7 exhibits the neutral stability curves for $\omega = 10$ and for different values of ϵ. Critical values are tabulated in Table 8 for the upper branch and Table 9 for the lower branch. The pattern of graphs is the same as that for $\omega = 7.9$. Our results indicate that as ϵ increases, the marginal stability curves shift to the left, and the critical Reynolds number Rdecreases, thus indicating a more unstable flow situation.

The wave-angle stability curves are depicted in Figs. 5(c), 6(c), 7(c) for $\omega = 4$, 7.9, and 10, respectively. These figures show that a broad range of negative wave-angle occurs for the lower branch as ϵ increases. Increases in ϵ and frequency ω cause bifurcation on the upper branch. Whereas for the stationary waves the lower-branch is affected significantly with increasing ϵ, for the non-stationary waves the upper-branch is more affected, particularly for large Reynolds numbers. The upper-branch behaviour is governed by the dynamics of the critical layers where the mean flow velocity is equal to the phase velocity. With the flow velocity being concentrated closer to the wall for increasing ϵ, this is therefore likely to affect more the lower frequency waves rather than the higher frequency waves, as the critical layer positions will move closer to the wall. This behaviour is consistent with that seen in Fig. 5 for $\omega = 4$ and Figs. 6 and 7 for the higher frequencies.

We have also plotted the growth rate curves for selected Reynolds numbers. Fig. 8 displays the distribution of the spatial amplification rate of zero-frequency

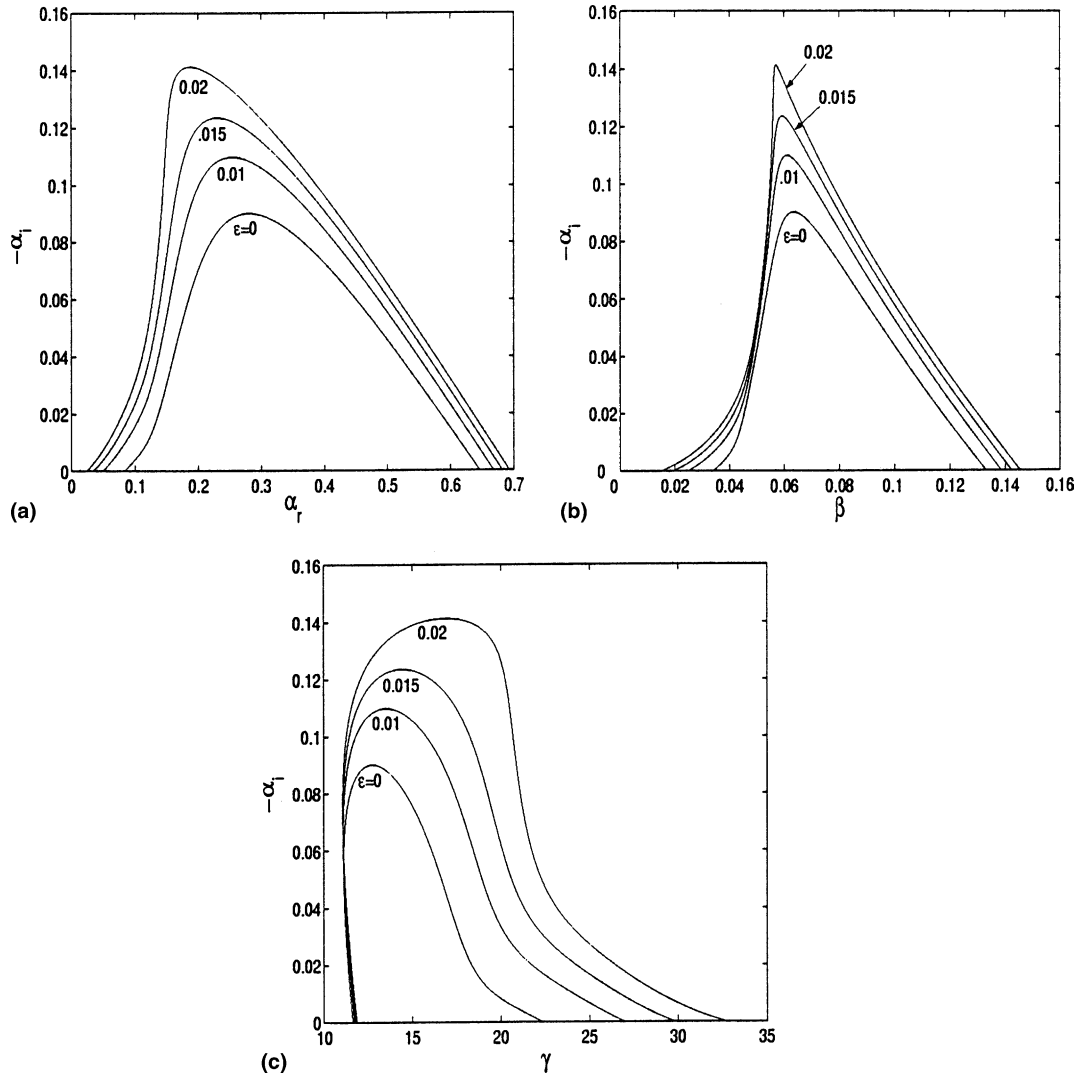

Fig. 8. Distribution of the spatial amplication rate of stationary waves as a function of wavenumbers (a) (α_i, α_r), (b) (α_i, β), and wave-angle (c) (α_i, γ) for $R = 600$ and different values of ϵ.

as a function of wavenumbers (α_i, α_r), (α_i, β), and wave-angle (α_i, γ) when $R = 600$, for several values of ϵ. Fig. 8(c) gives the orientations of the stationary waves versus the spatial growth rate. On the lower branch, the growing waves originate almost from the same place at a wave-angle. On the upper branch, amplifying waves originate at a larger wave-angle as Rincreases. With ϵ varying from zero to 0.03, the growth rates of travelling waves with a frequency of 10 are shown in Fig. 9 for $R = 600$. These graphs suggest that travelling waves, for ϵ non-zero have smaller growth rates than stationary waves, a conclusion quite different from that for the constant viscosity case. Also, due to viscous mode instability (lower branch) at lower Reynolds numbers, the eigenvalues ranges separate into two distinct regions, which is characteristic of non-zero frequency waves of the rotating disk flow. The wave orientation for travelling waves is shown in Fig. 9(c). For $\epsilon = 0$, the values we obtain agree quite well with those derived earlier by TG.

3.3. Absolute instability results

Following the procedure developed by TG, we have computed the branch points of the flow for different values of viscosity variation parameter ϵ with Prandtl number taken equal to 0.72. Our results show that the rotating disk boundary layer flow with temperature-dependent viscosity exhibits both convective and absolute instabilities in some regions of the flow. Using the Newton–Raphson search procedure (see TG), we have

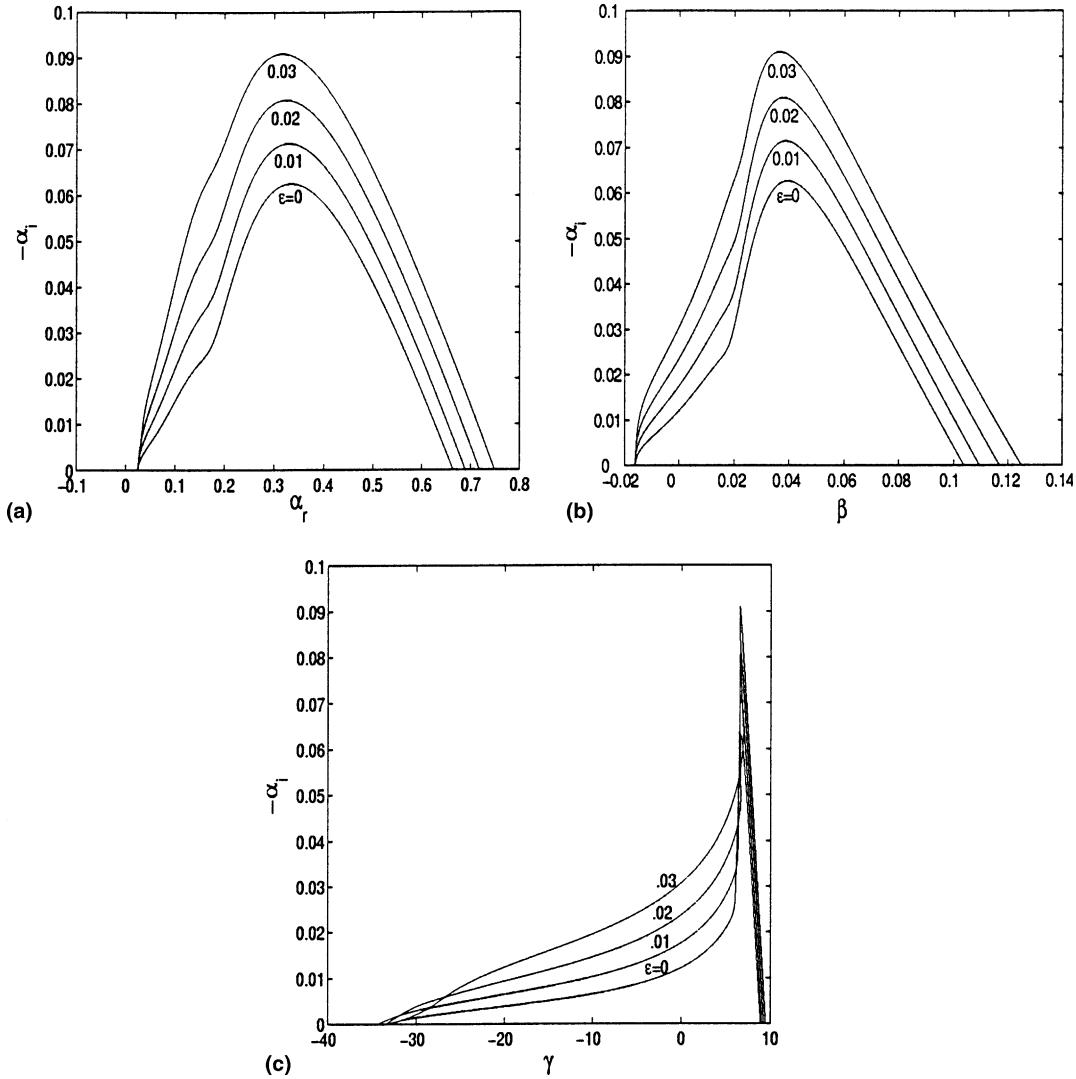

Fig. 9. Distribution of the spatial amplication rate of travelling waves with $\omega = 10$ as a function of wavenumbers (a) (α_i, α_r), (b) (α_i, β), and wave-angle (c) (α_i, γ) for $R = 600$ and different values of ϵ.

solved the eight-order system of equations, and the branch points are found for the viscous solution. The Briggs [25] criterion has been employed with fixed parameters β and R to distinguish between absolutely and convectively unstable flows.

Fig. 10 shows the parameter range of neutral absolute instability in the (R,α_r), (R,α_i), (R,β), (R,ω_r), and (R,γ) planes for different values of ϵ. Inside the curves, the imaginary part of the frequency ω is positive and thus the particular flow there is absolutely unstable. Outside the curves, the flow becomes convectively unstable. Table 10 displays the computed values of the critical Reynolds number R, corresponding critical wavenumbers α, β, frequency ω, and wave-angle γ when different value of viscosity variation parameter ϵ are taken into account. Table 10 shows that as ϵ increases, the critical

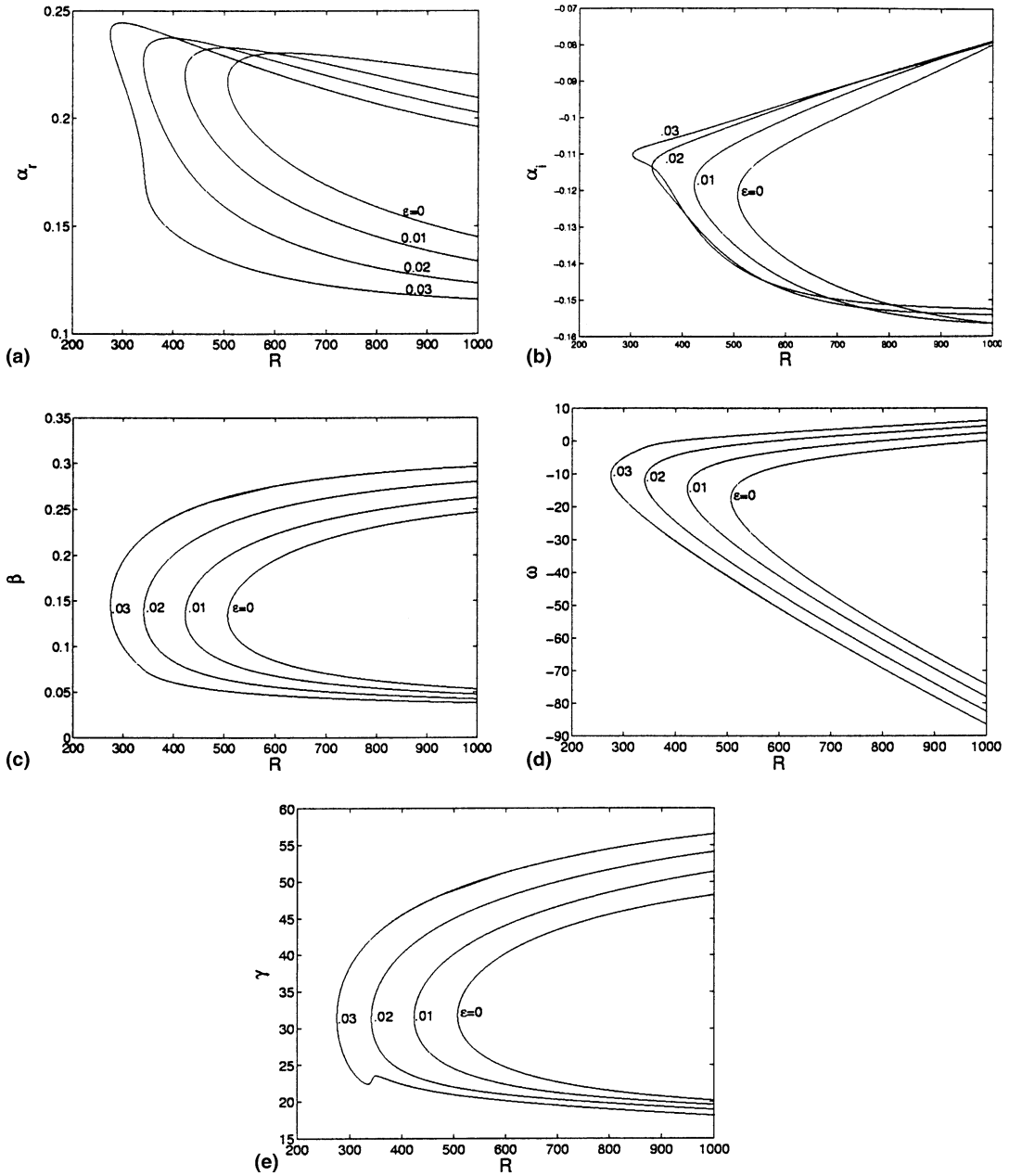

Fig. 10. Neutral absolute instability curves in (a) (R,α_r), (b) (R,α_i), (c) (R,β), (d) (R,ω_r), and (e) (R,γ) wavenumber, frequency, and wave-angle planes for different values of ϵ.

Table 10
Critical values of R, α, β, ω_r, and γ corresponding to different values of ϵ for the absolute instability curves

ϵ	R	α_r	α_i	β	ω_r	γ
0	507.0	0.216	−0.121	0.134	−17.27	31.50
0.01	423.0	0.220	−0.118	0.135	−14.60	31.52
0.02	341.0	0.226	−0.113	0.138	−12.01	31.53
0.03	275.1	0.239	−0.107	0.147	−10.58	31.54

Reynolds number R for the onset of absolute instability decreases such that the absolutely unstable region increases. For $\epsilon = 0$, the eigenvalues we obtain agree quite well with those derived earlier by TG and Lingwood [23]. The flows become much more absolutely unstable as the viscosity variation parameter ϵ increases.

4. Conclusions

The influence of temperature dependent viscosity on a rotating disk in a rigidly rotating fluid have been investigated using linear stability theory. The primary flow is affected through the variation of viscosity with temperature. The stability parameters for the stationary and non-stationary waves are computed.

Using a spectral method, stability diagrams are produced for different values of the viscosity variation parameter ϵ with the Prandtl number taken equal to 0.72 (suitable for air). Neutral stability curves are sketched for various real frequencies and several values of the viscosity variation parameter ϵ. The region enclosed by these curves is shown to be convectively unstable. Positive frequency causes the critical Reynolds number for the onset of convective instability on the lower branch to decrease and that on the upper branch to increase. Increase in the viscosity variation parameter ϵ leads to decrease in the critical Reynolds number for both branches. Since the viscosity is more sensitive to temperature as ϵ increases, the rotating-disk flow is much more unstable.

We have also investigated the absolute instability with several values of e. A linear stability analysis has been performed including viscous, Coriolis and streamline curvature effects. A branch of the dispersion relation has been shown to meet the upper branch at a pinch-point with positive ω_i. Neutral stability curves are presented which display the absolute unstable, convective unstable and stable regions for several values of ϵ. All the curves inside the loop signify absolute instability, while outside convective stability/instability. It is significant to note that as ϵ is increased, the critical value of the Reynolds number for absolute instability decreases and the flow becomes increasingly unstable. We have shown also that for the convectively unstable modes, stationary waves have larger growth rates as compared to the non-stationary waves for large Reynolds numbers.

Although the non-parallel approximation has been used in the stability analysis, the behaviour of the stability loops for increasing ϵ suggests that non-parallel effects will be important for $\epsilon > 0$. The low values of the critical Reynolds numbers obtained in this study for ϵ increasing may invalidate the earlier large Reynolds number assumptions made in obtaining the stability equations. This however, requires a study of the full linearized unsteady Navier–Stokes equation, which is beyond the scope of the present paper.

In many experiments on cross-flow instability the variation of viscosity with temperature is usually neglected. Our results demonstrate the results can be particularly sensitive to very small changes in viscosity with temperature.

References

[1] T. Von-Kármán, Uber laminare und turbulente reibung, Z. Angew. Math. Mech. 1 (1921) 233–252.
[2] W.G. Cochran, The flow due to a rotating disc, Proc. Cambridge Phil. Soc. 30 (1934) 365–375.
[3] U.T. Bödewadt, Die drehströmung iiber festem grand, Z. Angew. Math. Mech. 20 (1940) 241–253.
[4] M.H. Rogers, G.N. Lance, The rotationally symmetric flow of a viscous fluid in the presence of an infinite rotating disc, J. Fluid Mech. 7 (1960) 617–631.
[5] E.M. Sparrow, J.L. Gregg, Heat transfers from a rotating disc to a fluid any Prandtl number, ASME J. Heat Tran. 81 (1959) 249–251.
[6] J.P. Hartnett, Heat transfer from a non-isothermal rotating disc in still air, ASME J. Appl. Mech. 4 (1959) 672–673.
[7] J. Gary, D.R. Kassoy, H. Tadjeran, A. Zebib, The effect of significant viscosity variation on convective heat transport in water-saturated porous media, J. Fluid Mech. 117 (1982) 233–249.
[8] K.N. Mehta, S. Sood, Transient free convection flow with temperature dependent viscosity in fluid saturated porous medium, Int. J. Eng. Sci. 30 (1992) 1083–1087.
[9] N.G. Kafoussias, E.W. Williams, The effect of temperature dependent viscosity on the free convective laminar boundary layer flow past a vertical isothermal flat plate, Acta Mech. 110 (1995) 123–137.
[10] N.G. Kafoussias, D.A.S. Rees, Numerical studies of the combined free and forced convective laminar boundary layer flow past a vertical isothermal flat plate with temperature dependent viscosity, Acta Mech. 127 (1998) 39–50.
[11] H.B. Keller, Numerical methods in the boundary layer theory, Ann. Rev. Mech. 10 (1978) 417–433.
[12] M.A. Hossain, A. Hossain, M. Wilson, Unsteady flow of viscous incompressible fluid with temperature-dependent viscosity due to a rotating disc in presence of transverse magnetic field and heat transfer, Int. J. Therm. Sci. 40 (2001) 11–20.

[13] D.P. Wall, S.K. Wilson, The linear stability of channel flow of fluid with temperature-dependent viscosity, J. Fluid Mech. 323 (1996) 107–132.
[14] A. Pinarbasi, C. Ozalp, Effect of viscosity models on the stability of a non-Newtonian fluid in a channel with heat transfer, Int. Commun. Heat Mass 28 (2001) 369–378.
[15] V.M. Shevtsova, D.E. Melnikov, J.C. Legros, Three-dimensional simulations of hydrodynamic instability in liquid bridges: influence of temperature-dependent viscosity, Phys. Fluids 13 (2001) 2851–2865.
[16] M.A. Hossain, M.S. Munir, M.Z. Hafiz, H.S. Takhar, Flow of viscous incompressible fluid of temperature dependent viscosity past a permeable wedge with uniform surface heat flux, Heat Mass Transfer 36 (2000) 333–341.
[17] K.T.R. Chang, K.P. Chen, Linear stability of mixed convection flow of two immiscible fluids in a vertical annulus, J. Heat Trans-T ASME 123 (2001) 434–440.
[18] I.S. Mckinlay, S.K. Wilson, The linear stability of a ridge of fluid subject to a jet of air, Phys. Fluids 13 (2001) 872–883.
[19] M.A. Hossain, S. Kabir, D.A.S. Rees, Natural convection of fluid with variable viscosity from a heated vertical wavy surface, Z. Angew. Math. Phys. 53 (2002) 48–57.
[20] S. Ferro, G. Gnavi, Effects of temperature-dependent viscosity in channels with porous walls, Phys. Fluids 14 (2002) 829–849.
[21] J.X. Ling, A. Dybbs, Forced convection over a flat plate submersed in a porous medium: variable viscosity case, ASME Paper 87-WA/TH-23. (1987) 1–7.
[22] M. Turkyilmazoglu, J.S.B. Gajjar, Absolute and convective instability in the incompressible boundary layer on a rotating disk, Report no. CLSCM, 1998, University of Manchester.
[23] R.J. Lingwood, Absolute instability of the boundary layer on a rotating-disk, J. Fluid Mech. 299 (1995) 17–33.
[24] P. Hall, An asymptotic investigation of the stationary modes of instability of the boundary layer on a rotating-disk, Proc. Roy. Soc. London Ser. A 406 (1986) 93–106.
[25] R.J. Briggs, Electron–Stream Interaction with Plasmas, MIT Press, 1964.